Self-energy pole optimization of superconductivity in the bilayer Hubbard model

Taka-Shi Fujiwara,[1] Shiro Sakai,[2] and Ryotaro Arita[1,3]

[1]*Department of Physics, The University of Tokyo, 7-3-1 Hongo, Bunkyo-ku, Tokyo 113-0033, Japan*
[2]*Physics Division, Sophia University, Chiyoda-ku, Tokyo 102-8554, Japan*
[3]*RIKEN Center for Emergent Matter Science, 2-1 Hirosawa, Wako, Saitama 351-0198, Japan*

(Dated: July 28, 2026)

We study the real-frequency structure of the self-energy in the bilayer Hubbard model, using the dynamical cluster approximation. At half filling, the Mott insulator–band insulator (MI–BI) crossover involves a rearrangement of self-energy poles between the bonding and antibonding bands; these poles cross as the interlayer hopping $t_\perp$ is varied. Upon doping, this pole structure produces a band-selective pseudogap and enhances $s^\pm$-wave superconductivity. The order parameter is maximized near the MI–BI boundary, where low-energy anomalous self-energy poles develop simultaneously in both bands and cooperatively enhance the pairing. We further show that these self-energy poles can be interpreted as emergent fermionic excitations, offering an enhanced-pairing mechanism in common with the single-layer Hubbard model. The controllability of these poles through $t_\perp$ makes the bilayer system an unconventional platform for optimizing strongly correlated superconductivity.

Introduction. In strongly correlated electron systems, the electron self-energy can have a nontrivial frequency dependence beyond a mere renormalization of the quasiparticle mass: its low-energy poles reshape the single-particle excitation spectrum, producing features such as the Mott gap and pseudogap. When superconductivity occurs due to the strong correlations, the dynamical structure of the anomalous self-energy—not just its static value—controls the pairing strength [1–5], signaling the underlying unconventional mechanism, just as in conventional superconductors, where the analysis of the frequency dependence identified their phonon-mediated mechanism [6–8].

Such physics is most pronounced near a Mott insulator, where strong correlations generate a large self-energy with marked momentum and frequency dependence—a picture widely invoked for the pseudogap and superconductivity in underdoped cuprates [9–12]. Indeed, cluster dynamical mean-field studies of the single-layer Hubbard model have found that self-energy poles inherited from the Mott insulator govern the low-energy dynamics of both the pseudogap and the superconducting states [3–5, 13–18]. In particular, the poles of the anomalous self-energy enhance the pairing [1, 5]. In the single-layer model, however, the pole position is mostly determined by the interaction strength and the doping level [17], leaving little room for tuning it to strengthen superconductivity.

Recently, the bilayer Hubbard model has attracted renewed attention as another simple model accommodating strongly correlated superconductivity [19–28], especially in light of the pressure-induced high-T_c superconductivity in the bilayer nickelate $La_3Ni_2O_7$ [29] and the subsequent experimental [30–38] and theoretical studies [39–56]. In this model, the interlayer hopping $t_\perp$ splits the spectrum into bonding and antibonding bands and controls unconventional pairing channels. The model is known to host a Mott insulator–band insulator (MI–BI) crossover at half filling [57, 58], as well as pseudogap behavior [28, 59, 60] and $s^\pm$-wave superconductivity with a rather high critical temperature [28, 42, 43, 46, 47, 56, 60–63] upon light hole doping. However, its superconducting mechanism has been mainly discussed in terms of weak-coupling theory, where the shape of the Fermi surfaces (i.e., poles of the Green's function) is a key parameter [42, 43, 46, 47, 56, 61, 62].

In this work, we demonstrate a Mott-physics-driven high-temperature superconducting mechanism, which is controllable through $t_\perp$, in the small doping region of the bilayer Hubbard model. We compute the real-frequency self-energy, using the dynamical cluster approximation [64, 65] combined with exact diagonalization (DCA+ED). At half filling, the MI–BI crossover [57, 58] appears as a spectral reconstruction accompanied by a rearrangement of self-energy poles between the bonding and antibonding bands. These poles move through the low-energy region and cross each other as $t_\perp$ is varied. Upon doping, this structure develops into band-selective pseudogaps in the normal state and enhances an $s^\pm$-wave superconducting state. In the latter case, the order parameter is maximized near the MI–BI boundary, where the self-energy poles of both bands simultaneously reach low energy and cooperatively enhance the superconductivity. We show that the low-energy structure of the self-energy is quantitatively reproduced by a hidden-fermion model [5, 17, 66] extended to the bilayer system, identifying the low-energy poles as emergent fermionic excitations, common to those in the single-layer Hubbard model. The controllability of the self-energy poles through $t_\perp$ in the bilayer model provides a microscopic handle for designing correlated superconductivity.

Model and method. We consider the bilayer Hubbard model on a square lattice, which reads

$$\mathcal{H} = -t \sum_{\langle i,j\rangle,l,\sigma} c^\dagger_{il\sigma} c_{jl\sigma} - t_\perp \sum_{i,l\neq l',\sigma} c^\dagger_{il\sigma} c_{il'\sigma} + U \sum_{i,l} n_{il\uparrow} n_{il\downarrow}. \quad (1)$$

Here, i and j label lattice sites, $l, l' = 1, 2$ are layers, and $\sigma = \uparrow, \downarrow$ are spins. The parameters t ($t_\perp$) and U denote

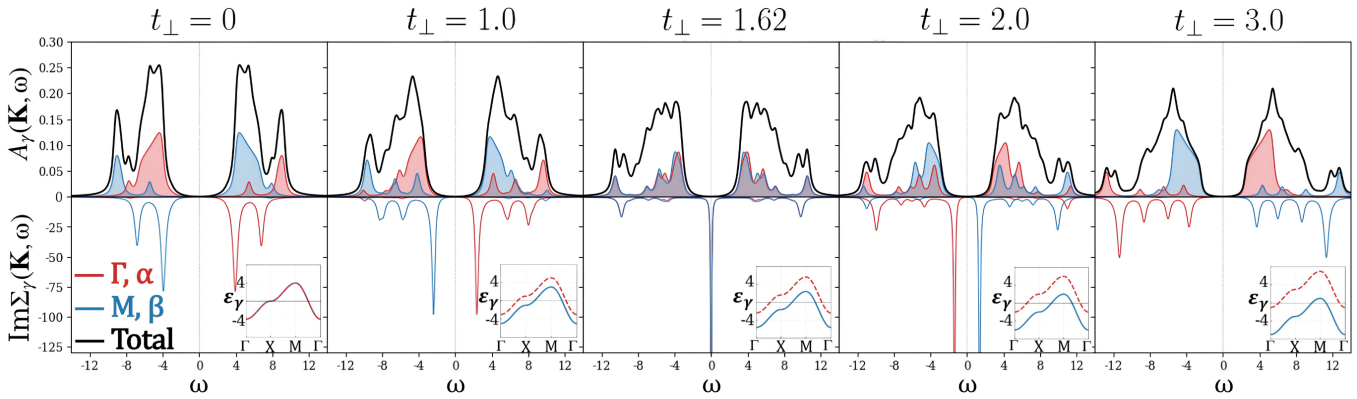

FIG. 1. Spectral function $A_\gamma(\mathbf{K},\omega)$ (top row) and imaginary part of the normal self-energy $\mathrm{Im}\,\Sigma_\gamma^{\mathrm{nor}}(\mathbf{K},\omega)$ (bottom row) at half filling ($\delta = 0$) and $U = 12$ for $t_\perp = 0$, 1.0, 1.62, 2.0, and 3.0 (left to right). Red and blue curves denote the Γ-α and M-β components; the black curve in the top row is the total DOS. The poles of $\mathrm{Im}\,\Sigma_\gamma^{\mathrm{nor}}$, located inside the Mott gap, cross around $t_\perp \simeq t_{\perp,c} \simeq 1.62$, identifying the MI–BI crossover as a rearrangement of these poles between the two components. Insets in the lower panels show the bare ($U = 0$) band dispersions $\varepsilon_\gamma(\mathbf{k})$ along Γ-X-M-Γ.

the intralayer (interlayer) nearest-neighbor hopping and the onsite Coulomb repulsion, respectively. We set $t = 1$ as the energy unit and take $t_\perp > 0$ throughout the paper. The chemical potential μ controls the hole-doping concentration δ w.r.t. half filling.

Introducing the bonding–antibonding basis between the layers, $c_{i\sigma}^{\alpha} = \frac{1}{\sqrt{2}}(c_{i1\sigma} - c_{i2\sigma})$ and $c_{i\sigma}^{\beta} = \frac{1}{\sqrt{2}}(c_{i1\sigma} + c_{i2\sigma})$, we obtain the band dispersions $\varepsilon_{\alpha,\beta}(\mathbf{k}) = -2t(\cos k_x + \cos k_y) \pm t_\perp - \mu$ for $U = 0$. Hereafter, we specify the band with $\gamma \in \{\alpha, \beta\}$, where α and β denote the antibonding and bonding bands, respectively.

To treat short-range correlations and symmetry breaking, we employ the dynamical cluster approximation (DCA) [64, 65]. In DCA, the Brillouin zone is divided into patches centered at cluster momenta $\mathbf{K}$, and the lattice problem is mapped onto a finite cluster impurity problem through the coarse-grained Green's function

$$\bar{G}_\gamma(\mathbf{K},\omega) = \frac{N_c}{2N}\sum_{\tilde{\mathbf{k}}} G_\gamma(\mathbf{K}+\tilde{\mathbf{k}},\omega). \tag{2}$$

Here, N denotes the number of lattice sites in each layer, N_c is the number of sites in a cluster, and $\tilde{\mathbf{k}}$ runs over the $2N/N_c$ momentum points in each patch. Besides the layers, we take two cluster momenta $\mathbf{K} = (0,0)$ and (π,π) ($N_c = 4$ in total), around which separate Fermi surfaces formed by the α and β bands reside for $U = 0$ and $0 < t_\perp < 4$. We label these low-energy components Γ-$\alpha \equiv (\mathbf{k} = (0,0), \alpha)$ and M-$\beta \equiv (\mathbf{k} = (\pi,\pi), \beta)$.

The four-site interacting cluster problem with eight noninteracting bath sites is solved by the Lanczos method [67], which can yield real-frequency Green's functions directly via continued-fraction expansions [68], without analytic continuation from the Matsubara axis. The bath parameters are determined self-consistently, with an artificial temperature $T = t/200$, which is low enough to effectively yield the ground state.

In the superconducting state, the normal Green's function is written as

$$G_\gamma(\mathbf{k},\omega) = \left[\omega - \varepsilon_\gamma(\mathbf{k}) - \Sigma_\gamma^{\mathrm{nor}}(\mathbf{k},\omega) - W_\gamma(\mathbf{k},\omega)\right]^{-1}, \tag{3}$$

where $\Sigma_\gamma^{\mathrm{nor}}(\mathbf{k},\omega)$ is the normal self-energy and

$$W_\gamma(\mathbf{k},\omega) = \left[\Sigma_\gamma^{\mathrm{ano}}(\mathbf{k},\omega)\right]^2 / \left(\omega + \varepsilon_\gamma(\mathbf{k}) + \Sigma_\gamma^{\mathrm{nor}}(\mathbf{k},-\omega)^*\right) \tag{4}$$

represents the feedback of the anomalous self-energy $\Sigma_\gamma^{\mathrm{ano}}(\mathbf{k},\omega)$ on $G_\gamma(\mathbf{k},\omega)$. The superconducting gap appearing in the spectral function $A_\gamma(\mathbf{K},\omega) = -(1/\pi)\mathrm{Im}\bar{G}_\gamma(\mathbf{K},\omega)$ is thus determined by the total self-energy $\Sigma_\gamma^{\mathrm{nor}} + W_\gamma$. We substitute the self-energy, $\Sigma_\gamma^{\mathrm{nor}}(\mathbf{K},\omega)$ and $\Sigma_\gamma^{\mathrm{ano}}(\mathbf{K},\omega)$, at cluster momenta into Eqs. (3) and (4) to obtain $\bar{G}_{\gamma\sigma}$ and W_γ.

Spectra at half filling. Figure 1 shows the spectral functions and normal self-energies at half filling ($\delta = 0$) and $U = 12$ for various values of $t_\perp$. At $t_\perp = 0$, the two layers are decoupled, and the system reduces to the single-layer Hubbard model in the Mott-insulating regime. In this case, the spectral weight around the Fermi level is strongly suppressed due to the poles of $\Sigma_\gamma^{\mathrm{nor}}$, which appear as sharp peaks of $\mathrm{Im}\,\Sigma_\gamma^{\mathrm{nor}}$ in our results. As the self-energy pole of Γ-α (M-β) is located on the unoccupied (occupied) side, the spectral weight of Γ-α (M-β) is pronounced on the occupied (unoccupied) side.

As $t_\perp$ increases, the spectral center of Γ-α (M-β) shifts upward (downward) owing to the increasing bonding–antibonding splitting. Concomitantly, the self-energy pole of Γ-α (M-β) inside the gap shifts downward (upward), crossing each other at $t_\perp \simeq t_{\perp,c}$, where $t_{\perp,c} \simeq 1.62$ for $U = 12$. For $t_\perp > t_{\perp,c}$, they retreat from low energy, and the spectra become band-insulator-like, dominated by the bonding–antibonding splitting. Thus, the MI–BI crossover at half filling [57, 58] does not involve a gap closing but a spectral rearrangement between the Γ-α and M-β components. Crucially, the controllability of

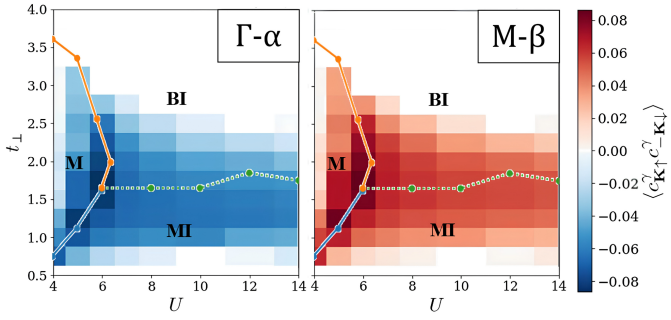

FIG. 2. Superconducting order parameters in the $(U, t_\perp)$ plane at $\delta = 0.02$: $\langle c^\alpha_{\Gamma\uparrow} c^\alpha_{\Gamma\downarrow}\rangle$ for the Γ-α component (left) and $\langle c^\beta_{\mathrm{M}\uparrow} c^\beta_{\mathrm{M}\downarrow}\rangle$ for the M-β component (right), on a common color scale. The opposite signs (Γ-$\alpha < 0$: blue, M-$\beta > 0$: red) indicate $s^\pm$-wave symmetry. The phase diagram at half filling is superimposed (M: metal, MI: Mott insulator, BI: band insulator; the MI–BI boundary is determined in Sec. S5). Both components are largest near the MI–BI boundary and peak toward the metallic region.

these self-energy poles by $t_\perp$, uncovered here at half filling, carries over to the doped region and governs the pseudogap and superconducting states there, as we shall see in the following.

Pseudogap state. At small doping ($\delta = 0.02$), we find band-selective pseudogaps by constraining the solution to the normal state. The spectra at $U = 12$ are shown in Sec. S2 of the Supplemental Material. For $t_\perp = 1 \lesssim t_{\perp,c}$, the M-$\beta$ (Γ-α) component is gapped (gapless) [59]. For $t_\perp = 2 \gtrsim t_{\perp,c}$, the gapped (gapless) component switches to Γ-α (M-β) [28, 60]. Thus, in the lightly hole-doped regime, two types of band-selective pseudogaps emerge, reflecting the self-energy poles that remain on the occupied side at half filling: an M-β (Γ-α)-selective one for $t_\perp \lesssim t_{\perp,c}$ ($t_\perp \gtrsim t_{\perp,c}$). This component selectivity is characteristic of the bilayer system and is inherited by the anomalous self-energy in the superconducting state.

Superconducting order parameter. Figure 2 shows the $(U, t_\perp)$ map of the order parameters at $\delta = 0.02$ for the Γ-α and M-β components, with the half-filling phase diagram superimposed. The two components have opposite signs and approximately satisfy $\langle c^\alpha_{\Gamma\uparrow} c^\alpha_{\Gamma\downarrow}\rangle \simeq -\langle c^\beta_{\mathrm{M}\uparrow} c^\beta_{\mathrm{M}\downarrow}\rangle$, consistent with the $s^\pm$-wave symmetry, with a sign change between the Γ-α and M-β components [28, 60].

This $s^\pm$-wave superconductivity emerges mainly in the $(U, t_\perp)$ region where the self-energy poles generating the Mott gap reside at low energy for both components at half filling (see Fig. 1). Accordingly, the magnitude of the order parameter becomes large for both components near the MI–BI boundary, where these two poles approach and cross each other at low energy. This enhancement is therefore tied to the self-energy poles present at half filling and persisting at low energy even after doping. Moreover, along the MI–BI boundary, the order parameter is maximized near the boundary with the metallic region at half filling. This is likely because the poles of

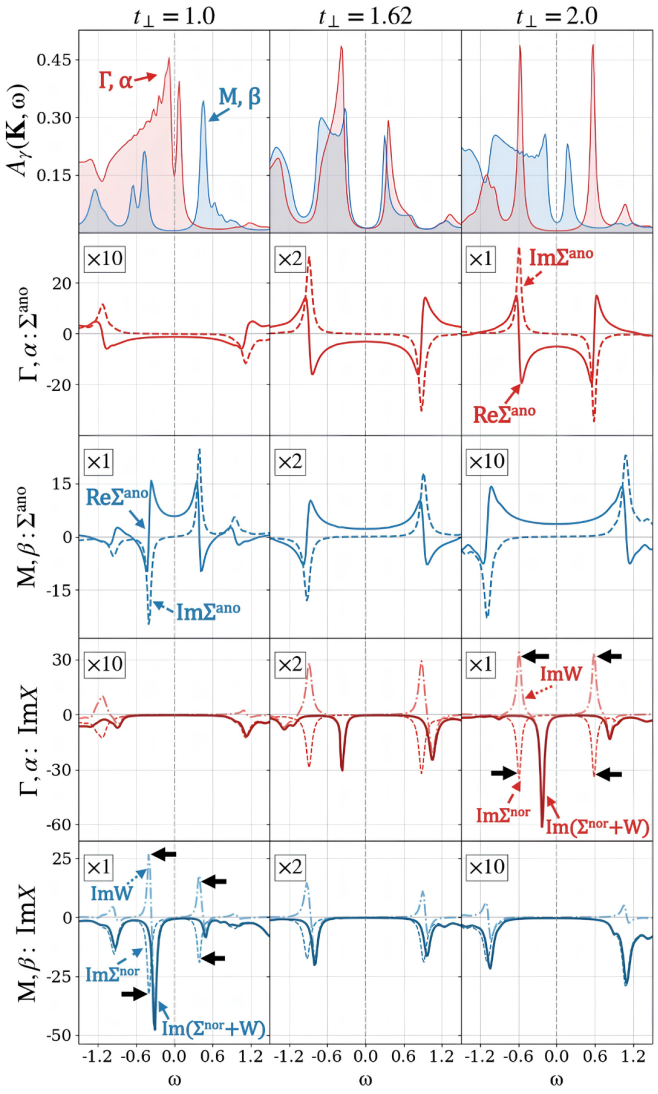

FIG. 3. Real-frequency results in the superconducting state at $U = 12$ and $\delta = 0.02$ for $t_\perp = 1.0$, $1.62\,(\simeq t_{\perp,c})$, and 2.0 (left to right). From top to bottom: spectral function $A_\gamma(\mathbf{K}, \omega)$ (Γ-α: red, M-β: blue); anomalous self-energy $\Sigma^{\mathrm{ano}}_\gamma(\mathbf{K}, \omega)$ for Γ-α and then M-β (solid: $\mathrm{Re}\,\Sigma^{\mathrm{ano}}$, dashed: $\mathrm{Im}\,\Sigma^{\mathrm{ano}}$); and $\mathrm{Im}\,X_\gamma$ for Γ-α and then M-β with $X \in \{\Sigma^{\mathrm{nor}}, W, \Sigma^{\mathrm{nor}} + W\}$ ($\mathrm{Im}\,\Sigma^{\mathrm{nor}}_\gamma$: dashed, $\mathrm{Im}\,W_\gamma$: dash-dotted, sum: solid). Per-panel scale factors (except A_γ) are given in the upper-left corner. Black arrows mark the pole-to-pole cancellation between $\Sigma^{\mathrm{nor}}_\gamma$ and W_γ, derived analytically in Sec. S3.

both components, originally located inside a narrow gap at half filling, remain very close to the Fermi level upon doping and efficiently enhance pair formation, as we shall discuss in the following.

Real-frequency spectra in the superconducting state. Figure 3 shows A_γ, $\Sigma^{\mathrm{ano}}_\gamma$, and $\mathrm{Im}\,W_\gamma$ in the superconducting state at $U = 12$ and $\delta = 0.02$. We compare the representative values $t_\perp = 1.0$, $1.62\,(\simeq t_{\perp,c})$, and 2.0, which straddle the pole crossing at half filling. We find that a superconducting gap opens in both the Γ-α and M-β

components for all these values of $t_\perp$, and that anomalous self-energy poles stand out at particle-hole symmetric energies in both components.

As in the pseudogap state, the structure of the self-energy poles at half filling (Fig. 1) is carried over into the superconducting state for $\delta > 0$, not only in the normal but also in the anomalous component. For $t_\perp = 1 < t_{\perp,c}$, the M-$\beta$ pole dominates the low-energy region after doping; for $t_\perp = 2 > t_{\perp,c}$, the Γ-α pole dominates instead. At $t_\perp \simeq t_{\perp,c}$, both poles are around zero energy at half filling. This generates pronounced low-energy poles in $\Sigma_\gamma^{\rm ano}$ for both Γ-α and M-β after hole doping, though the poles slightly shift away from the Fermi energy due to the hole doping.

These poles strongly enhance the static pairing strength $\mathrm{Re}\,\Sigma_\gamma^{\rm ano}(\mathbf{K}, \omega = 0)$ through the Kramers–Kronig relation

$$\mathrm{Re}\,\Sigma_\gamma^{\rm ano}(\mathbf{K}, \omega = 0) = \frac{2}{\pi}\int_0^\infty d\omega\, \frac{\mathrm{Im}\,\Sigma_\gamma^{\rm ano}(\mathbf{K}, \omega)}{\omega}, \qquad (5)$$

and thereby enhance the superconducting gap [1]. Since the integrand on the r.h.s. of Eq. (5) is weighted by $1/\omega$, a pole closer to $\omega = 0$ gives a larger contribution. At $t_\perp \simeq t_{\perp,c}$, such low-energy poles exist simultaneously in both Γ-α and M-β components, and hence $\mathrm{Re}\,\Sigma_\gamma^{\rm ano}(0)$ is enhanced for both. This directly produces the order-parameter maximum in Fig. 2: the cooperative growth of both superconducting gaps strengthens the $s^\pm$ order near the MI–BI boundary.

As shown in the lower panels of Fig. 3, a nontrivial cancellation occurs between $\mathrm{Im}\,\Sigma_\gamma^{\rm nor}$ and $\mathrm{Im}\,W_\gamma$ in the superconducting state: Although both $\Sigma_\gamma^{\rm nor}$ and W_γ exhibit pole structures, a pole disappears in their sum and hence in the Green's function. This pole-to-pole cancellation has also been observed in the single-layer Hubbard model [5, 18], where it indicates that the poles of the normal and anomalous self-energies share the same origin. This cancellation does not occur for a self-energy peak generated by bosonic excitations and instead suggests a coupling to an emergent fermionic excitation [5, 69, 70], as discussed in the following; see Sec. S3 of the Supplemental Material for details.

Hidden-fermion fitting. To interpret the DCA self-energies, we employ a minimal phenomenological model in which the physical electron c hybridizes with an emergent fermionic degree of freedom f [5, 17, 66]:

$$\begin{aligned}\mathcal{H}^{\rm HF} = &\sum_{\mathbf{k},\gamma,\sigma}\left[(\varepsilon_{c,\gamma}(\mathbf{k}) + s_{\gamma\mathbf{k}})c^{\gamma\dagger}_{\mathbf{k}\sigma}c^{\gamma}_{\mathbf{k}\sigma} + \varepsilon_{f,\gamma}(\mathbf{k})f^{\gamma\dagger}_{\mathbf{k}\sigma}f^{\gamma}_{\mathbf{k}\sigma}\right]\\ &+ \sum_{\mathbf{k},\gamma,\sigma} V_{\gamma\mathbf{k}}\left(c^{\gamma\dagger}_{\mathbf{k}\sigma}f^{\gamma}_{\mathbf{k}\sigma} + \mathrm{H.c.}\right)\\ &- \sum_{\mathbf{k},\gamma}\left(D_{c,\gamma\mathbf{k}}c^{\gamma\dagger}_{\mathbf{k}\uparrow}c^{\gamma\dagger}_{\mathbf{k}\downarrow} + D_{f,\gamma\mathbf{k}}f^{\gamma\dagger}_{\mathbf{k}\uparrow}f^{\gamma\dagger}_{\mathbf{k}\downarrow} + \mathrm{H.c.}\right). \qquad (6)\end{aligned}$$

Here, $\varepsilon_{c,\gamma}$ and $\varepsilon_{f,\gamma}$ denote the dispersions of the c and f fermions, respectively, $s_{\gamma\mathbf{k}}$ is the energy shift emerging from the electron correlation, $V_{\gamma\mathbf{k}}$ is their hybridization, and $D_{c,\gamma\mathbf{k}}$ and $D_{f,\gamma\mathbf{k}}$ are their anomalous terms.

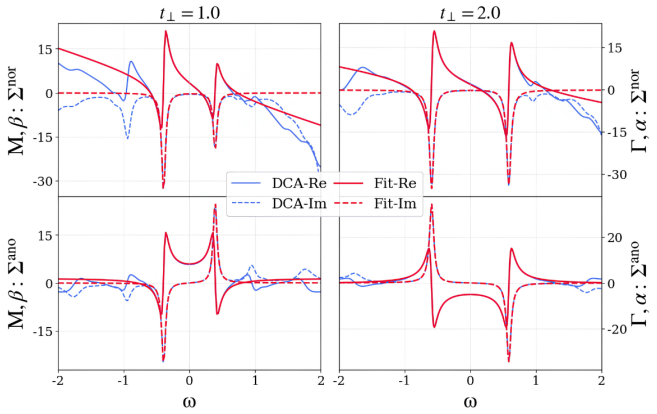

FIG. 4. Hidden-fermion fit of $\Sigma_\gamma^{\rm nor}(\mathbf{K}, \omega)$ (top) and $\Sigma_\gamma^{\rm ano}(\mathbf{K}, \omega)$ (bottom) at $U = 12$ and $\delta = 0.02$: the M-β component at $t_\perp = 1.0$ (left) and the Γ-α component at $t_\perp = 2.0$ (right). Blue curves are the DCA data and red curves are the fitting with the hidden-fermion model [Eqs. (7) and (8)]; solid and dashed curves denote real and imaginary parts. A single low-energy hidden fermion reproduces the pole structure of both channels.

Integrating out the f degrees of freedom, we obtain the self-energies for the c fermion as

$$\Sigma_\gamma^{\rm nor}(\mathbf{k}, \omega) = s_{\gamma\mathbf{k}} + \frac{V_{\gamma\mathbf{k}}^2(\omega + \varepsilon_{f,\gamma}(\mathbf{k}))}{\omega^2 - \varepsilon_{f,\gamma}(\mathbf{k})^2 - D_{f,\gamma\mathbf{k}}^2}, \qquad (7)$$

$$\Sigma_\gamma^{\rm ano}(\mathbf{k}, \omega) = D_{c,\gamma\mathbf{k}} - \frac{V_{\gamma\mathbf{k}}^2 D_{f,\gamma\mathbf{k}}}{\omega^2 - \varepsilon_{f,\gamma}(\mathbf{k})^2 - D_{f,\gamma\mathbf{k}}^2}. \qquad (8)$$

These equations show the poles of $\Sigma_\gamma^{\rm nor}$ and $\Sigma_\gamma^{\rm ano}$ at the same particle-hole symmetric energies $\omega = \pm\sqrt{\varepsilon_{f,\gamma}(\mathbf{k})^2 + D_{f,\gamma\mathbf{k}}^2}$.

Figure 4 shows the fitting of the DCA self-energies by Eqs. (7) and (8) for $t_\perp = 1.0 < t_{\perp,c}$ and for $t_\perp = 2.0 > t_{\perp,c}$ at $\delta = 0.02$. The low-energy pole structures obtained by DCA are accurately reproduced in both $\Sigma_\gamma^{\rm nor}$ and $\Sigma_\gamma^{\rm ano}$. This almost perfect fitting at low energies supports the picture that a quasiparticle hybridizes with the emergent fermionic degree of freedom f_γ.

The best fitting is obtained at $(\varepsilon_{f,\gamma}(\mathbf{k}),\, D_{f,\gamma\mathbf{k}},\, |V_{\gamma\mathbf{k}}|) = (-0.106,\, 0.378,\, 1.36)$ for M-β at $t_\perp = 1.0$ and $(-0.011,\, -0.589,\, 1.67)$ for Γ-α at $t_\perp = 2.0$. Since $|\varepsilon_{f,\gamma}| \lesssim 0.1$, the corresponding pole energies are $E_\gamma = \sqrt{\varepsilon_{f,\gamma}^2 + D_{f,\gamma\mathbf{k}}^2} \simeq |D_{f,\gamma\mathbf{k}}| = 0.39$ and 0.59, respectively. These are much smaller than $U = 12t$ and the bandwidth $W = 8t + 2t_\perp$, placing the poles deep inside the low-energy window. The subdominant high-energy corrections are detailed in Sec. S4.

The hidden-fermion model explains the pole-to-pole cancellation, as derived analytically in Sec. S3 of the Supplemental Material. The quality of the fitting, together with the consistency with this analytical result, strongly supports the conclusion that the self-energy poles originate from a hidden-fermion degree of freedom.

Similar hidden-fermion models have been shown to quantitatively reproduce the self-energy of the single-layer repulsive Hubbard model, as well as of the strong-coupling attractive Hubbard model [17, 18, 71], where electrons form strongly bound Cooper pairs. The applicability of the hidden-fermion model in the present bilayer system therefore indicates the presence of strongly bound Cooper pairs, which are presumably formed between the layers in this system. The hidden fermion supplies both the pseudogap and enhanced superconductivity through the hybridization with low-energy electrons, acting as a unified mechanism for the two phenomena. Specific to the bilayer system, $t_\perp$ acts as an external knob to control the dispersion of the hidden fermion, allowing us to optimize the $s^\pm$ pairing.

Summary. Using DCA+ED, we clarified the real-frequency structure of the self-energy in the bilayer Hubbard model. At half filling, the MI–BI crossover with varying $t_\perp$ is accompanied by the crossing of the self-energy poles of the Γ-α and M-β components. Upon hole doping, the two different configurations of the self-energy poles produce different band-selective pseudogaps in the normal state: an M-β (Γ-α)-selective one for $t_\perp \lesssim t_{\perp,c}$ ($t_\perp \gtrsim t_{\perp,c}$). In the superconducting state, the self-energy poles stabilize $s^\pm$-wave pairing with opposite signs in the two components. The order parameter is maximized near the MI–BI boundary, where the self-energy poles located at low energies reinforce the pairing for both Γ-α and M-β.

We have shown that the self-energy structure admits a hidden-fermion interpretation common to the strongly correlated superconductivity in the single-layer Hubbard model, with a crucial difference specific to the bilayer: $t_\perp$ acts as an external knob on the pole positions and hence on the pairing strength. The bilayer structure thus offers an unprecedented route to optimizing strongly correlated superconductivity. In systems that realize a single-orbital bilayer Hubbard model near half filling—such as bilayer optical-lattice fermions or suitably engineered bilayer materials—these predictions could be tested directly: ARPES should resolve the band-selective pseudogap that switches between the bonding and antibonding sheets across $t_\perp \simeq t_{\perp,c}$, and tuning $t_\perp$ should trace the maximization of the pairing near the MI–BI boundary. A quantitative description of the multiorbital nickelate $La_3Ni_2O_7$, which lies away from this regime, is left for future work.

Acknowledgments— We thank Yusuke Nomura for a useful discussion. This work is supported by Grant-in-Aid for Scientific Research from JSPS, KAKENHI Grant No. 25H01252, No. 24H00190, No. 26K00650, JST K-Program JPMJKP25Z7, RIKEN TRIP initiative (RIKEN Quantum, Advanced General Intelligence for Science Program, Many-body Electron Systems).

[1] T. A. Maier, D. Poilblanc, and D. J. Scalapino, Phys. Rev. Lett. **100**, 237001 (2008).
[2] B. Kyung, D. Sénéchal, and A.-M. S. Tremblay, Phys. Rev. B **80**, 205109 (2009).
[3] M. Civelli, Phys. Rev. Lett. **103**, 136402 (2009).
[4] E. Gull and A. J. Millis, Phys. Rev. B **91**, 085116 (2015).
[5] S. Sakai, M. Civelli, and M. Imada, Phys. Rev. Lett. **116**, 057003 (2016).
[6] G. M. Eliashberg, Sov. Phys. JETP **11**, 696 (1960).
[7] W. L. McMillan and J. M. Rowell, Phys. Rev. Lett. **14**, 108 (1965).
[8] D. J. Scalapino, J. R. Schrieffer, and J. W. Wilkins, Phys. Rev. **148**, 263 (1966).
[9] P. W. Anderson, Science **235**, 1196 (1987).
[10] B. Keimer, S. A. Kivelson, M. R. Norman, S. Uchida, and J. Zaanen, Nature **518**, 179 (2015).
[11] P. A. Lee, N. Nagaosa, and X.-G. Wen, Rev. Mod. Phys. **78**, 17 (2006).
[12] D. J. Scalapino, Rev. Mod. Phys. **84**, 1383 (2012).
[13] T. D. Stanescu and G. Kotliar, Phys. Rev. B **74**, 125110 (2006).
[14] S. Sakai, Y. Motome, and M. Imada, Phys. Rev. Lett. **102**, 056404 (2009).
[15] E. Gull, O. Parcollet, and A. J. Millis, Phys. Rev. Lett. **110**, 216405 (2013).
[16] G. Sordi, P. Sémon, K. Haule, and A.-M. S. Tremblay, Phys. Rev. Lett. **108**, 216401 (2012).
[17] S. Sakai, M. Civelli, and M. Imada, Phys. Rev. B **94**, 115130 (2016).
[18] S. Sakai, M. Civelli, and M. Imada, Phys. Rev. B **98**, 195109 (2018).
[19] N. Bulut, D. J. Scalapino, and R. T. Scalettar, Phys. Rev. B **45**, 5577 (1992).
[20] R. T. Scalettar, J. W. Cannon, D. J. Scalapino, and R. L. Sugar, Phys. Rev. B **50**, 13419 (1994).
[21] R. E. Hetzel, W. von der Linden, and W. Hanke, Phys. Rev. B **50**, 4159 (1994).
[22] R. R. dos Santos, Phys. Rev. B **51**, 15540 (1995).
[23] A. I. Liechtenstein, I. I. Mazin, and O. K. Andersen, Phys. Rev. Lett. **74**, 2303 (1995).
[24] K. Bouadim, G. G. Batrouni, F. Hébert, and R. T. Scalettar, Phys. Rev. B **77**, 144527 (2008).
[25] N. Lanatà, P. Barone, and M. Fabrizio, Phys. Rev. B **80**, 224524 (2009).
[26] T. A. Maier and D. J. Scalapino, Phys. Rev. B **84**, 180513 (2011).
[27] T. A. Maier, V. Mishra, G. Balduzzi, and D. J. Scalapino, Phys. Rev. B **99**, 140504 (2019).
[28] S. Karakuzu, S. Johnston, and T. A. Maier, Phys. Rev. B **104**, 245109 (2021).
[29] H. Sun, M. Huo, X. Hu, J. Li, Z. Liu, Y. Han, L. Tang, Z. Mao, P. Yang, B. Wang, J. Cheng, D.-X. Yao, G.-M. Zhang, and M. Wang, Nature **621**, 493 (2023).
[30] J. Hou, P.-T. Yang, Z.-Y. Liu, J.-Y. Li, P.-F. Shan, L. Ma, G. Wang, N.-N. Wang, H.-Z. Guo, J.-P. Sun, Y. Uwatoko, M. Wang, G.-M. Zhang, B.-S. Wang, and J.-G. Cheng, Chin. Phys. Lett. **40**, 117302 (2023).
[31] G. Wang, N. N. Wang, X. L. Shen, J. Hou, L. Ma, L. F. Shi, Z. A. Ren, Y. D. Gu, H. M. Ma, P. T. Yang, Z. Y. Liu, H. Z. Guo, J. P. Sun, G. M. Zhang, S. Calder, J.-Q.

Yan, B. S. Wang, Y. Uwatoko, and J.-G. Cheng, Phys. Rev. X **14**, 011040 (2024).
[32] Y. Zhang, D. Su, Y. Huang, Z. Shan, H. Sun, M. Huo, K. Ye, J. Zhang, Z. Yang, Y. Xu, Y. Su, R. Li, M. Smidman, M. Wang, L. Jiao, and H. Yuan, Nat. Phys. **20**, 1269 (2024).
[33] N. Wang, G. Wang, X. Shen, J. Hou, J. Luo, X. Ma, H. Yang, L. Shi, J. Dou, J. Feng, J. Yang, Y. Shi, Z. Ren, H. Ma, P. Yang, Z. Liu, Y. Liu, H. Zhang, X. Dong, Y. Wang, K. Jiang, J. Hu, S. Nagasaki, K. Kitagawa, S. Calder, J. Yan, J. Sun, B. Wang, R. Zhou, Y. Uwatoko, and J. Cheng, Nature **634**, 579 (2024).
[34] E. K. Ko, Y. Yu, Y. Liu, L. Bhatt, J. Li, V. Thampy, C.-T. Kuo, B. Y. Wang, Y. Lee, K. Lee, J.-S. Lee, B. H. Goodge, D. A. Muller, and H. Y. Hwang, Nature **638**, 935 (2025).
[35] G. Zhou, W. Lv, H. Wang, Z. Nie, Y. Chen, Y. Li, H. Huang, W.-Q. Chen, Y.-J. Sun, Q.-K. Xue, and Z. Chen, Nature **640**, 641 (2025).
[36] Y. Liu, E. K. Ko, Y. Tarn, L. Bhatt, J. Li, V. Thampy, B. H. Goodge, D. A. Muller, S. Raghu, Y. Yu, and H. Y. Hwang, Nat. Mater. **24**, 1221 (2025).
[37] B. Hao, M. Wang, W. Sun, Y. Yang, Z. Mao, S. Yan, H. Sun, H. Zhang, L. Han, Z. Gu, J. Zhou, D. Ji, and Y. Nie, Nat. Mater. **24**, 1756 (2025).
[38] F. Li, Z. Xing, D. Peng, J. Dou, N. Guo, L. Ma, Y. Zhang, L. Wang, J. Luo, J. Yang, J. Zhang, T. Chang, Y.-S. Chen, W. Cai, J. Cheng, Y. Wang, Y. Liu, T. Luo, N. Hirao, T. Matsuoka, H. Kadobayashi, Z. Zeng, Q. Zheng, R. Zhou, Q. Zeng, X. Tao, and J. Zhang, Nature **649**, 871 (2026).
[39] Z. Luo, X. Hu, M. Wang, W. Wú, and D.-X. Yao, Phys. Rev. Lett. **131**, 126001 (2023).
[40] V. Christiansson, F. Petocchi, and P. Werner, Phys. Rev. Lett. **131**, 206501 (2023).
[41] F. Lechermann, J. Gondolf, S. Bötzel, and I. M. Eremin, Phys. Rev. B **108**, L201121 (2023).
[42] Y.-B. Liu, J.-W. Mei, F. Ye, W.-Q. Chen, and F. Yang, Phys. Rev. Lett. **131**, 236002 (2023).
[43] Q.-G. Yang, D. Wang, and Q.-H. Wang, Phys. Rev. B **108**, L140505 (2023).
[44] Z. Liao, L. Chen, G. Duan, Y. Wang, C. Liu, R. Yu, and Q. Si, Phys. Rev. B **108**, 214522 (2023).
[45] Y. Zhang, L.-F. Lin, A. Moreo, T. A. Maier, and E. Dagotto, Nat. Commun. **15**, 2470 (2024).
[46] G. Heier, K. Park, and S. Y. Savrasov, Phys. Rev. B **109**, 104508 (2024).
[47] S. Bötzel, F. Lechermann, J. Gondolf, and I. M. Eremin, Phys. Rev. B **109**, L180502 (2024).
[48] S. Ryee, N. Witt, and T. O. Wehling, Phys. Rev. Lett. **133**, 096002 (2024).
[49] K. Jiang, Z. Wang, and F.-C. Zhang, Chin. Phys. Lett. **41**, 017402 (2024).
[50] Z. Luo, B. Lv, M. Wang, W. Wú, and D.-X. Yao, npj Quantum Mater. **9**, 61 (2024).
[51] C. Lu, Z. Pan, F. Yang, and C. Wu, Phys. Rev. Lett. **132**, 146002 (2024).
[52] K.-Y. Jiang, Y.-H. Cao, Q.-G. Yang, H.-Y. Lu, and Q.-H. Wang, Phys. Rev. Lett. **134**, 076001 (2025).
[53] Y.-H. Tian, Y. Chen, J.-M. Wang, R.-Q. He, and Z.-Y. Lu, Phys. Rev. B **109**, 165154 (2024).
[54] Z. Fan, J.-F. Zhang, B. Zhan, D. Lv, X.-Y. Jiang, B. Normand, and T. Xiang, Phys. Rev. B **110**, 024514 (2024).
[55] Y. Gu, C. Le, Z. Yang, X. Wu, and J. Hu, Phys. Rev. B **111**, 174506 (2025).
[56] H. Sakakibara, N. Kitamine, M. Ochi, and K. Kuroki, Phys. Rev. Lett. **132**, 106002 (2024).
[57] S. S. Kancharla and S. Okamoto, Phys. Rev. B **75**, 193103 (2007).
[58] H. Lee, Y.-Z. Zhang, H. O. Jeschke, and R. Valentí, Phys. Rev. B **89**, 035139 (2014).
[59] L. Fratino, S. Bag, A. Camjayi, M. Civelli, and M. Rozenberg, Phys. Rev. B **105**, 125140 (2022).
[60] Y. Nomura, M. Kitatani, S. Sakai, and R. Arita, Phys. Rev. B **112**, L020504 (2025).
[61] K. Kuroki, T. Kimura, and R. Arita, Phys. Rev. B **66**, 184508 (2002).
[62] V. Mishra, D. J. Scalapino, and T. A. Maier, Sci. Rep. **6**, 32078 (2016).
[63] D. Kato and K. Kuroki, Phys. Rev. Research **2**, 023156 (2020).
[64] M. H. Hettler, A. N. Tahvildar-Zadeh, M. Jarrell, T. Pruschke, and H. R. Krishnamurthy, Phys. Rev. B **58**, R7475 (1998).
[65] T. Maier, M. Jarrell, T. Pruschke, and M. H. Hettler, Rev. Mod. Phys. **77**, 1027 (2005).
[66] S. Sakai, J. Phys. Soc. Jpn. **92**, 092001 (2023).
[67] M. Caffarel and W. Krauth, Phys. Rev. Lett. **72**, 1545 (1994).
[68] E. R. Gagliano and C. A. Balseiro, Phys. Rev. Lett. **59**, 2999 (1987).
[69] Y. Yamaji and M. Imada, Phys. Rev. Lett. **106**, 016404 (2011).
[70] M. Imada and T. J. Suzuki, J. Phys. Soc. Jpn. **88**, 024701 (2019).
[71] S. Sakai, M. Civelli, Y. Nomura, and M. Imada, Phys. Rev. B **92**, 180503 (2015).

Supplemental Material for "Self-energy pole optimization of superconductivity in the bilayer Hubbard model"

Taka-Shi Fujiwara, Shiro Sakai, and Ryotaro Arita

S1. COMPUTATIONAL DETAILS OF THE DCA SCHEME

A. Momentum-space coarse graining

In the dynamical cluster approximation (DCA) [1, 2], the lattice self-energy is approximated by a function that is piecewise constant in momentum,

$$\Sigma_\gamma(\mathbf{k},\omega) \simeq \Sigma_\gamma(\mathbf{K},\omega) \qquad (\mathbf{k}\in P_{\mathbf{K}}), \tag{S1}$$

where $P_{\mathbf{K}}$ denotes the patch surrounding the cluster momentum $\mathbf{K}$. The Brillouin zone is partitioned into patches of equal area centered at the cluster momenta, and the lattice degrees of freedom inside each patch are coarse grained according to Eq. (2).

For the present bilayer calculations, we use the two cluster momenta $\mathbf{K} = (0,0)$ and (π,π), so that the in-plane Brillouin zone is divided into the two patches sketched in Fig. S1: the central region around $\mathbf{K} = (0,0)$, which contains the α-band Fermi surface, and the corner region around $\mathbf{K} = (\pi,\pi)$, which contains the β-band Fermi surface. Together with the two layers, this amounts to $N_c = 4$ cluster orbitals. Because each patch is dominated by a single low-energy band, the coarse graining directly realizes the band–momentum combined labels Γ-α and M-β used throughout the main text.

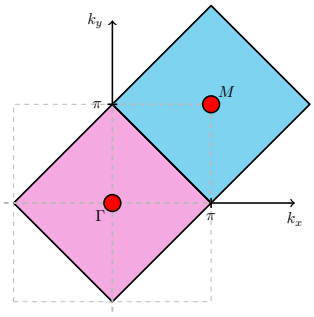

FIG. S1. Partition of the in-plane Brillouin zone into the two DCA patches used in this work, centered at the cluster momenta $\mathbf{K} = (0,0)$ and (π,π). The patch around $(0,0)$ contains the α (antibonding) Fermi surface and the patch around (π,π) contains the β (bonding) Fermi surface, defining the Γ-α and M-β components. Within each patch the self-energy is approximated as $\mathbf{k}$-independent [Eq. (S1)].

B. Exact-diagonalization (ED) impurity solver

The cluster problem obtained after the coarse graining is represented by the $N_c = 4$ interacting cluster orbitals coupled to $N_b = 8$ noninteracting bath sites, and is solved by the Lanczos method at an artificial inverse temperature $\beta = 200$, which practically yields the ground-state result. This method allows the cluster Green's function and self-energy to be evaluated directly on the real-frequency axis through a continued-fraction expansion [3], without the analytic continuation from the Matsubara-frequency axis required by quantum Monte Carlo solvers; this is essential for resolving the low-energy self-energy poles of interest here.

In each self-consistency cycle, the bath parameters—the bath levels and the cluster–bath hybridizations—are determined by fitting the cluster Weiss field $\mathcal{G}_{0,\gamma}(\mathbf{K},\mathrm{i}\omega_n)$ with the finite bath. The bath parameters are optimized by minimizing the distance function

$$d = \sum_{\gamma,n} \left|\mathcal{G}_{0,\gamma}(\mathbf{K},\mathrm{i}\omega_n) - \mathcal{G}^{\mathrm{ED}}_{0,\gamma}(\mathbf{K},\mathrm{i}\omega_n)\right|^2, \tag{S2}$$

evaluated at the fermionic Matsubara frequencies $\omega_n = (2n-1)\pi T$, where $\mathcal{G}^{\mathrm{ED}}_{0,\gamma}$ is the Weiss field reproduced by the N_b bath sites.

Once the bath parameters are fixed, the discrete cluster impurity Hamiltonian H_{cl} is constructed, and its ground state $|\psi_0\rangle$ with energy E_0 is obtained by the Lanczos method. Because the diagonalization is carried out on the real-space cluster, the cluster Green's function is evaluated in the real-space–layer basis, in which $c_{il\sigma}$ ($c^\dagger_{il\sigma}$) annihilates (creates) an electron at cluster site i, layer l, and spin σ:

$$\begin{aligned} G^{ll'}_{\mathrm{cl},\sigma}(i,j;z) = {}& \langle\psi_0|\, c_{il\sigma}\, \frac{1}{z+E_0-H_{\mathrm{cl}}}\, c^\dagger_{jl'\sigma}\,|\psi_0\rangle \\ & + \langle\psi_0|\, c^\dagger_{jl'\sigma}\, \frac{1}{z-E_0+H_{\mathrm{cl}}}\, c_{il\sigma}\,|\psi_0\rangle. \end{aligned} \tag{S3}$$

Each resolvent is generated directly on the real-frequency axis as a continued fraction from the Lanczos tridiagonalization of H_{cl}. Taking the particle part of a diagonal element ($i = j$, $l = l'$) and starting from the seed state $|\phi_0\rangle = c^\dagger_{il\sigma}|\psi_0\rangle$, the tridiagonalization of H_{cl} in the Krylov space spanned by $\{H^n_{\mathrm{cl}}|\phi_0\rangle\}_{n=0,1,2,\cdots}$ generates the coefficients $\{a_n, b_n\}$, so that

$$\begin{aligned} & \langle\psi_0|\, c_{il\sigma}\, \frac{1}{z+E_0-H_{\mathrm{cl}}}\, c^\dagger_{il\sigma}\,|\psi_0\rangle \\ & \quad = \cfrac{\langle\phi_0|\phi_0\rangle}{z+E_0-a_0-\cfrac{b_1^2}{z+E_0-a_1-\cfrac{b_2^2}{z+E_0-a_2-\cdots}}}, \end{aligned} \tag{S4}$$

where $a_n = \langle\phi_n|H_{\mathrm{cl}}|\phi_n\rangle$ and b_n^2 are the squared off-diagonal Lanczos coefficients; the hole part and the

off-diagonal ($i \neq j$ or $l \neq l'$) elements are obtained analogously, and the anomalous components needed in the superconducting state are obtained in a similar way within the Nambu representation. The real-space–layer Green's function is finally Fourier transformed over the cluster sites and rotated into the bonding–antibonding basis [$c^{\alpha}_{i\sigma} = (c_{i1\sigma} - c_{i2\sigma})/\sqrt{2}$, $c^{\beta}_{i\sigma} = (c_{i1\sigma} + c_{i2\sigma})/\sqrt{2}$] to yield the band–cluster-momentum components $G_{\mathrm{cl},\gamma}(\mathbf{K}, z)$ used in the main text.

The cluster self-energy is then obtained from the Dyson equation $\Sigma_\gamma(\mathbf{K}, \mathrm{i}\omega_n) = \mathcal{G}_{0,\gamma}(\mathbf{K}, \mathrm{i}\omega_n)^{-1} - G_{\mathrm{cl},\gamma}(\mathbf{K}, \mathrm{i}\omega_n)^{-1}$, coarse grained through Eq. (2) to update $\bar{G}_\gamma$ and hence the Weiss field $\mathcal{G}^{-1}_{0,\gamma} = \bar{G}^{-1}_\gamma + \Sigma_\gamma$, and the loop is iterated until self-consistency is reached.

S2. PSEUDOGAP SPECTRA AT $\delta = 0.02$

This section presents the detailed spectra underlying the discussion of the band-selective pseudogap in the main text. Figure S2 shows the spectral functions $A_\gamma(\mathbf{K}, \omega)$ and the imaginary part of the normal self-energies $\mathrm{Im}\,\Sigma^{\mathrm{nor}}_\gamma(\mathbf{K}, \omega)$ obtained in the normal-state calculations at $U = 12$ and $\delta = 0.02$, for $t_\perp = 1.0$ (left) and $t_\perp = 2.0$ (right). On the Mott side ($t_\perp = 1.0$), the self-energy pole remaining near the occupied band suppresses the low-energy spectral weight of the M-β component and opens a pseudogap, while the Γ-α component stays gapless. On the band-insulator side ($t_\perp = 2.0$), the roles of the two components are interchanged, and the pseudogap opens in the Γ-α component.

S3. POLE-TO-POLE CANCELLATION IN THE HIDDEN-FERMION MODEL

In this section, we reproduce the pole-to-pole cancellation observed in the main text in terms of the hidden-fermion model [4]. The component index γ and the momentum $\mathbf{k}$ are suppressed below for brevity, and the fitting parameters are taken to be real, so that the complex conjugation in Eq. (4) is immaterial to the residue analysis. Retaining only the relevant low-energy pole, the normal and anomalous self-energies [Eqs. (7) and (8)] read

$$\Sigma^{\mathrm{nor}}(\omega) = s + \frac{V^2(\omega + \varepsilon_f)}{D(\omega)}, \tag{S5}$$

$$\Sigma^{\mathrm{ano}}(\omega) = D_c - \frac{V^2 D_f}{D(\omega)}, \tag{S6}$$

with the common denominator

$$D(\omega) \equiv \omega^2 - \varepsilon_f^2 - D_f^2. \tag{S7}$$

Both self-energies have simple poles at the particle-hole symmetric energies

$$\omega_{\mathrm{pole}} = \pm\sqrt{\varepsilon_f^2 + D_f^2}. \tag{S8}$$

Since $D(\omega) = (\omega - \omega_{\mathrm{pole}})(\omega + \omega_{\mathrm{pole}})$, one has $D'(\omega_{\mathrm{pole}}) = 2\omega_{\mathrm{pole}}$ and $1/D(\omega) \simeq [2\omega_{\mathrm{pole}}(\omega - \omega_{\mathrm{pole}})]^{-1}$, so that the residues of Eqs. (S5) and (S6) are

$$\mathrm{Res}[\Sigma^{\mathrm{nor}}, \omega_{\mathrm{pole}}] = \frac{V^2(\omega_{\mathrm{pole}} + \varepsilon_f)}{2\omega_{\mathrm{pole}}} \equiv R_n, \tag{S9}$$

$$\mathrm{Res}[\Sigma^{\mathrm{ano}}, \omega_{\mathrm{pole}}] = -\frac{V^2 D_f}{2\omega_{\mathrm{pole}}} \equiv R_a. \tag{S10}$$

We next examine the feedback term W of Eq. (4),

$$W(\omega) = \frac{[\Sigma^{\mathrm{ano}}(\omega)]^2}{\mathcal{D}_W(\omega)},$$
$$\mathcal{D}_W(\omega) \equiv \omega + \varepsilon_c + \Sigma^{\mathrm{nor}}(-\omega)^*. \tag{S11}$$

Using the evenness $D(-\omega) = D(\omega)$, the reflected normal self-energy reads

$$\Sigma^{\mathrm{nor}}(-\omega) = s + \frac{V^2(\varepsilon_f - \omega)}{D(\omega)}, \tag{S12}$$

which carries the *same* poles at $\omega = \omega_{\mathrm{pole}}$. Since the remaining terms of $\mathcal{D}_W$ are regular there, the residue of the denominator is (real, so the conjugation is irrelevant)

$$\mathrm{Res}[\mathcal{D}_W, \omega_{\mathrm{pole}}] = \frac{V^2(\varepsilon_f - \omega_{\mathrm{pole}})}{2\omega_{\mathrm{pole}}} \equiv R_d. \tag{S13}$$

Near $\omega = \omega_{\mathrm{pole}}$, the numerator of W thus diverges as $[\Sigma^{\mathrm{ano}}]^2 \sim R_a^2/(\omega - \omega_{\mathrm{pole}})^2$ while the denominator diverges as $\mathcal{D}_W \sim R_d/(\omega - \omega_{\mathrm{pole}})$, so their ratio retains only a *simple* pole,

$$W(\omega) \simeq \frac{R_a^2/(\omega - \omega_{\mathrm{pole}})^2}{R_d/(\omega - \omega_{\mathrm{pole}})} = \frac{R_a^2/R_d}{\omega - \omega_{\mathrm{pole}}} + \mathcal{O}(1), \tag{S14}$$

and hence

$$\mathrm{Res}[W, \omega_{\mathrm{pole}}] = \frac{R_a^2}{R_d} = \frac{V^2 D_f^2}{2\omega_{\mathrm{pole}}(\varepsilon_f - \omega_{\mathrm{pole}})}. \tag{S15}$$

We note that the regular (ω-finite) parts of Σ^{ano} and $\mathcal{D}_W$—including ε_c, the static shift s, and the high-energy corrections discussed in Sec. S4—contribute only to the $\mathcal{O}(1)$ background and drop out of the residue, so that $\mathrm{Res}[W, \omega_{\mathrm{pole}}]$ is fixed entirely by the hidden-fermion pole parameters through R_a and R_d.

Adding Eqs. (S9) and (S15), we obtain

$$\begin{aligned}
&\mathrm{Res}[\Sigma^{\mathrm{nor}} + W, \omega_{\mathrm{pole}}] \\
&= \frac{V^2(\omega_{\mathrm{pole}} + \varepsilon_f)}{2\omega_{\mathrm{pole}}} + \frac{V^2 D_f^2}{2\omega_{\mathrm{pole}}(\varepsilon_f - \omega_{\mathrm{pole}})} \\
&= \frac{V^2}{2\omega_{\mathrm{pole}}} \frac{(\omega_{\mathrm{pole}} + \varepsilon_f)(\varepsilon_f - \omega_{\mathrm{pole}}) + D_f^2}{\varepsilon_f - \omega_{\mathrm{pole}}} \\
&= \frac{V^2}{2\omega_{\mathrm{pole}}} \frac{\varepsilon_f^2 - \omega_{\mathrm{pole}}^2 + D_f^2}{\varepsilon_f - \omega_{\mathrm{pole}}} = 0,
\end{aligned} \tag{S16}$$

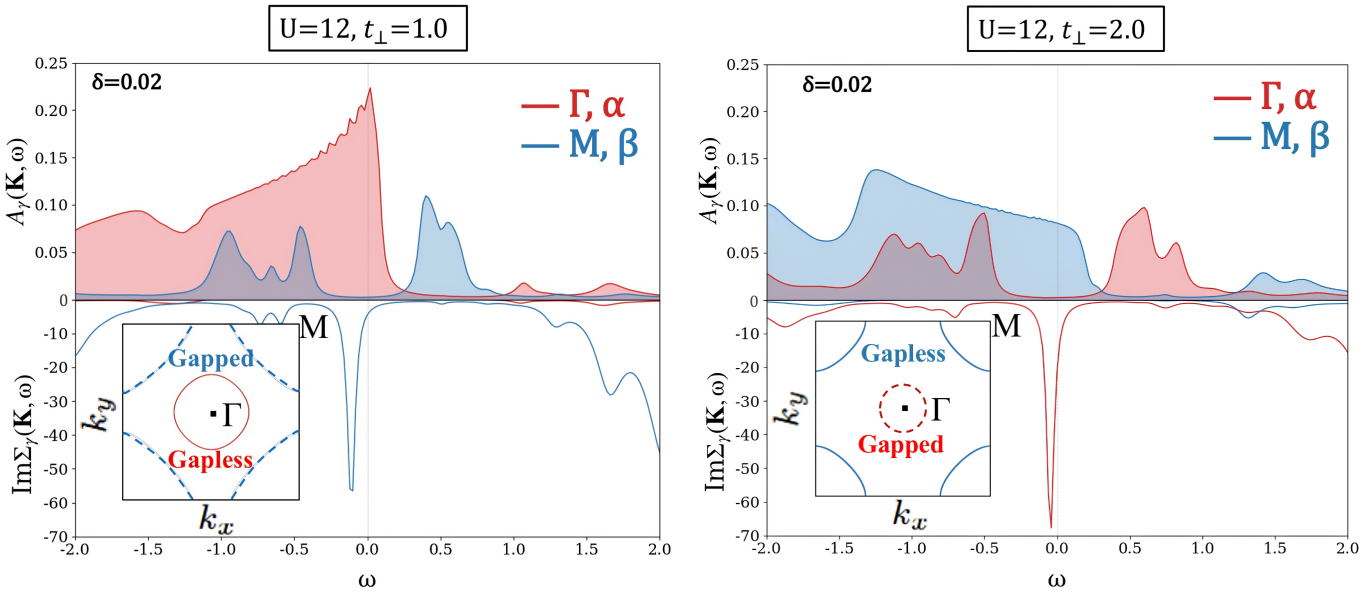

FIG. S2. Spectral function $A_\gamma(\mathbf{K},\omega)$ and the imaginary part of the normal self-energy $\mathrm{Im}\,\Sigma^{\mathrm{nor}}_\gamma(\mathbf{K},\omega)$ in the normal state at $U = 12$ and $\delta = 0.02$, for $t_\perp = 1.0$ (left) and $t_\perp = 2.0$ (right). A pseudogap opens in the M-β component for $t_\perp = 1.0$ and in the Γ-α component for $t_\perp = 2.0$, while the other component remains gapless. The insets to the bottom panels schematically illustrate the corresponding Fermi surfaces, where the gapped (gapless) component is drawn with a dashed (solid) curve.

where the numerator in the last line vanishes because $\varepsilon_f^2 + D_f^2 = \omega_{\mathrm{pole}}^2$. Thus, the poles of Σ^{nor} and W, originating from the same hidden-fermion degree of freedom, cancel exactly in the combination $\Sigma^{\mathrm{nor}} + W$ that enters the spectral function through Eq. (3). This analytically explains the disappearance of the singular structures in $\mathrm{Im}(\Sigma^{\mathrm{nor}} + W)$ observed numerically in Fig. 3. The same argument applies independently to the two poles $\omega_{\mathrm{pole}} = \pm\sqrt{\varepsilon_f^2 + D_f^2}$ and to each component γ.

S4. HIGH-ENERGY CORRECTIONS AND HIDDEN-FERMION FITTING PARAMETERS

A. General expression and high-energy corrections

In general, the self-energy of each component contains, besides the relevant low-energy pole, additional structures at higher energy. Because the hidden-fermion model of Eq. (6) focuses on the low-energy region, the effect of the high-energy structures should be incorporated in the model parameters [5, 6]. If we represent these high-energy structures with additional hidden fermions labeled by $\nu = 2, 3, \ldots$, we obtain

$$\Sigma^{\mathrm{nor}}_\gamma(\mathbf{k},\omega) = s_{\gamma\mathbf{k}} + \sum_\nu \frac{V^2_{\nu,\gamma\mathbf{k}}\,(\omega + \varepsilon_{f_\nu,\gamma}(\mathbf{k}))}{\omega^2 - \varepsilon_{f_\nu,\gamma}(\mathbf{k})^2 - D^2_{f_\nu,\gamma\mathbf{k}}}, \quad \text{(S17)}$$

$$\Sigma^{\mathrm{ano}}_\gamma(\mathbf{k},\omega) = D_{c,\gamma\mathbf{k}} - \sum_\nu \frac{V^2_{\nu,\gamma\mathbf{k}}\,D_{f_\nu,\gamma\mathbf{k}}}{\omega^2 - \varepsilon_{f_\nu,\gamma}(\mathbf{k})^2 - D^2_{f_\nu,\gamma\mathbf{k}}} \quad \text{(S18)}$$

in the same way as Eq. (6). Here, the $\nu = 1$ term is the low-energy pole retained in the main text, for which we abbreviate $\varepsilon_{f,\gamma}(\mathbf{k}) \equiv \varepsilon_{f_1,\gamma}(\mathbf{k})$, $D_{f,\gamma\mathbf{k}} \equiv D_{f_1,\gamma\mathbf{k}}$, and $V_{\gamma\mathbf{k}} \equiv V_{1,\gamma\mathbf{k}}$. We assume that the other poles ($\nu \geq 2$) lie at high energy, $E_{\nu,\gamma\mathbf{k}} \equiv \sqrt{\varepsilon_{f_\nu,\gamma}(\mathbf{k})^2 + D^2_{f_\nu,\gamma\mathbf{k}}}$, compared with the low-energy region $|\omega| \lesssim E_{1,\gamma\mathbf{k}}$ of interest. Expanding their contribution up to linear order in ω, we obtain

$$\sum_{\nu\geq 2} \frac{V^2_{\nu,\gamma\mathbf{k}}\,(\omega + \varepsilon_{f_\nu,\gamma}(\mathbf{k}))}{\omega^2 - E^2_{\nu,\gamma\mathbf{k}}} \simeq a_{\gamma\mathbf{k}} - b_{\gamma\mathbf{k}}\,\omega, \quad \text{(S19)}$$

$$-\sum_{\nu\geq 2} \frac{V^2_{\nu,\gamma\mathbf{k}}\,D_{f_\nu,\gamma\mathbf{k}}}{\omega^2 - E^2_{\nu,\gamma\mathbf{k}}} \simeq D_{\mathrm{HE},\gamma\mathbf{k}}, \quad \text{(S20)}$$

with

$$a_{\gamma\mathbf{k}} = -\sum_{\nu\geq 2} \frac{V^2_{\nu,\gamma\mathbf{k}}\,\varepsilon_{f_\nu,\gamma}(\mathbf{k})}{E^2_{\nu,\gamma\mathbf{k}}},$$

$$b_{\gamma\mathbf{k}} = \sum_{\nu\geq 2} \frac{V^2_{\nu,\gamma\mathbf{k}}}{E^2_{\nu,\gamma\mathbf{k}}},$$

$$D_{\mathrm{HE},\gamma\mathbf{k}} = \sum_{\nu\geq 2} \frac{V^2_{\nu,\gamma\mathbf{k}}\,D_{f_\nu,\gamma\mathbf{k}}}{E^2_{\nu,\gamma\mathbf{k}}}. \quad \text{(S21)}$$

Here $a_{\gamma\mathbf{k}}$ is an ω-independent shift, $b_{\gamma\mathbf{k}}$ renormalizes the c-fermion band, and $D_{\mathrm{HE},\gamma\mathbf{k}}$ is a static anomalous contribution from the high-energy poles. Combining these corrections with the $\nu = 1$ pole, the expressions used for

the actual fitting read

$$\Sigma_\gamma^{\rm nor}(\mathbf{k},\omega) \simeq \frac{V_{\gamma\mathbf{k}}^2\,(\omega+\varepsilon_{f,\gamma}(\mathbf{k}))}{\omega^2-\varepsilon_{f,\gamma}(\mathbf{k})^2-D_{f,\gamma\mathbf{k}}^2}+\tilde{a}_{\gamma\mathbf{k}}-b_{\gamma\mathbf{k}}\,\omega, \tag{S22}$$

$$\Sigma_\gamma^{\rm ano}(\mathbf{k},\omega) \simeq -\frac{V_{\gamma\mathbf{k}}^2\,D_{f,\gamma\mathbf{k}}}{\omega^2-\varepsilon_{f,\gamma}(\mathbf{k})^2-D_{f,\gamma\mathbf{k}}^2}+\tilde{D}_{{\rm HE},\gamma\mathbf{k}}, \tag{S23}$$

where the static shifts are collected into $\tilde{a}_{\gamma\mathbf{k}} \equiv a_{\gamma\mathbf{k}} + s_{\gamma\mathbf{k}}$ and $\tilde{D}_{{\rm HE},\gamma\mathbf{k}} \equiv D_{{\rm HE},\gamma\mathbf{k}} + D_{c,\gamma\mathbf{k}}$. For $\tilde{a}_{\gamma\mathbf{k}} = b_{\gamma\mathbf{k}} = \tilde{D}_{{\rm HE},\gamma\mathbf{k}} = 0$, Eqs. (S22) and (S23) reduce to the single-pole expressions of the main text, Eqs. (7) and (8).

B. Fitting procedure

The six parameters $\varepsilon_{f,\gamma}(\mathbf{k})$, $D_{f,\gamma\mathbf{k}}$, $V_{\gamma\mathbf{k}}$, $\tilde{a}_{\gamma\mathbf{k}}$, $b_{\gamma\mathbf{k}}$, and $\tilde{D}_{{\rm HE},\gamma\mathbf{k}}$ of each component are determined by a least-squares fit of the DCA+ED self-energies, using the same broadening as in the DCA+ED calculation, $\eta(\omega) = \eta_0 \min(10, 1+\omega^2)$ with $\eta_0 = 3\times10^{-2}$, which enters through the complex frequency $\omega \to \omega + {\rm i}\,\eta(\omega)$. The fit is restricted to the low-energy window in which the $\nu = 1$ pole is well separated from the higher-energy structures; outside this window additional poles enter the relevant range and the single-pole description breaks down. The fits shown in Fig. 4 of the main text are obtained in this way.

For the two fits shown in Fig. 4 of the main text, the high-energy correction parameters $(\tilde{a}_{\gamma\mathbf{k}}, b_{\gamma\mathbf{k}}, \tilde{D}_{{\rm HE},\gamma\mathbf{k}})$ are those listed in Table S1, namely, (2.10, 7.04, 1.41) for the M-β component at $t_\perp = 1.0$ and (1.83, 3.93, −0.33) for the Γ-α component at $t_\perp = 2.0$.

C. $t_\perp$ dependence of the hidden-fermion fit

Figure S3 demonstrates that the hidden-fermion model reproduces the DCA self-energies over the entire range of $t_\perp$, not only at a single value.

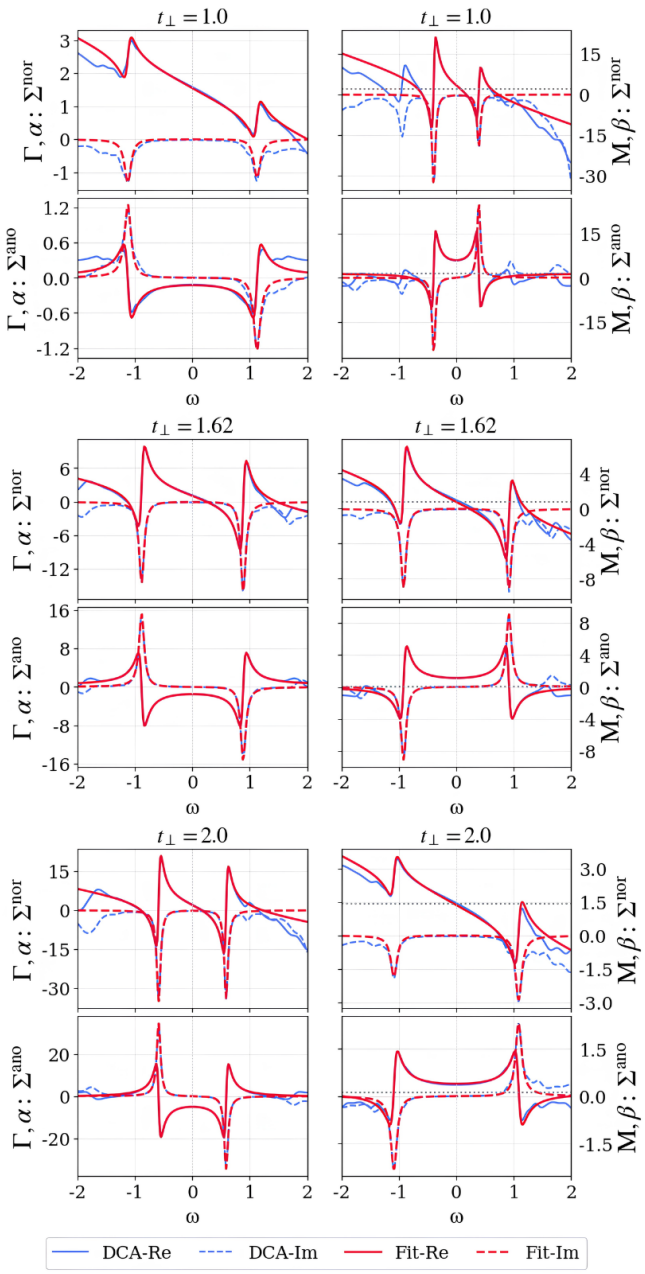

FIG. S3. Hidden-fermion fits of the normal ($\Sigma_\gamma^{\rm nor}$) and anomalous ($\Sigma_\gamma^{\rm ano}$) self-energies for the three representative interlayer hoppings $t_\perp = 1.0$, 1.62, and 2.0 (top, middle, and bottom blocks) at $U = 12$ and $\delta = 0.02$, straddling the pole crossing at half filling. Within each block the left (right) column shows the Γ-α (M-β) component, and the upper (lower) row shows $\Sigma_\gamma^{\rm nor}$ ($\Sigma_\gamma^{\rm ano}$). Blue curves are the DCA results and red curves the hidden-fermion fit [Eqs. (S22) and (S23)]; solid (dashed) curves denote the real (imaginary) part. The low-energy pole-like structures are reproduced for both components and both channels at every $t_\perp$. The fitting parameters are listed in Table S1.

We show $\Sigma_\gamma^{\rm nor}$ and $\Sigma_\gamma^{\rm ano}$ for both components $\gamma \in \{\alpha,\beta\}$ for $U = 12$ and $\delta = 0.02$ at the three representative interlayer hoppings $t_\perp = 1.0$, 1.62, and 2.0, which

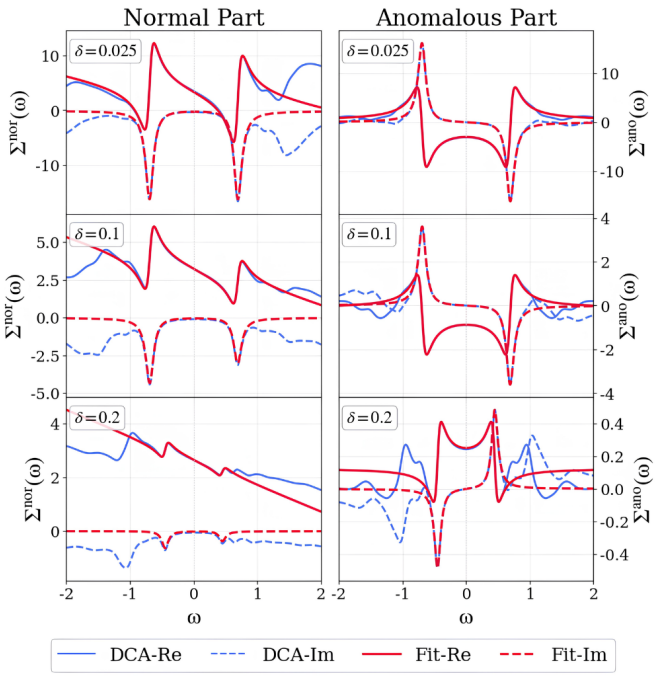

FIG. S4. Doping dependence of the hidden-fermion fit of the normal ($\Sigma_\gamma^{\rm nor}$, left column) and anomalous ($\Sigma_\gamma^{\rm ano}$, right column) self-energies of the Γ-α component at $U = 8$ and $t_\perp = 2.0$, for $\delta = 0.025$, 0.1, and 0.2 (top to bottom). Blue curves are the DCA results and red curves the hidden-fermion fit [Eqs. (S22) and (S23)]; solid (dashed) curves denote the real (imaginary) part. The fitting parameters are listed in Table S2. Note that the vertical scale differs between panels. With increasing doping, the pole structure associated with the hidden-fermion excitation weakens and, in the large-doping regime ($\delta = 0.2$), becomes buried among other structures of the self-energy.

straddle the pole crossing at half filling. For all $t_\perp$, the fit [Eqs. (S22) and (S23)] accurately captures the low-energy pole-like structures of both the real and imaginary parts of $\Sigma_\gamma^{\rm nor}$ and $\Sigma_\gamma^{\rm ano}$ in the Γ-α and M-β components alike. This systematic agreement, irrespective of $t_\perp$ and the component, shows that a single low-energy hidden-fermion pole per component suffices to describe the self-energy throughout the MI–BI crossover, and supports the picture that a quasiparticle in each component hybridizes with the emergent fermion f_γ across the whole parameter range.

The fitted pole position, read off from the pole energy $\pm\sqrt{\varepsilon_{f,\gamma}(\mathbf{k})^2 + D_{f,\gamma\mathbf{k}}^2}$ of each component, follows the pole motion discussed in the main text: on the MI side ($t_\perp = 1.0$) the M-β pole lies closest to $\omega = 0$, both poles approach low energy at $t_\perp = 1.62$, and on the BI side ($t_\perp = 2.0$) the Γ-α pole takes over the low-energy region.

D. Doping dependence of the hidden-fermion fit

The hidden-fermion description is rooted in the proximity to the Mott insulator, and is therefore expected to be most accurate at small doping and to deteriorate as the doping increases. To examine this trend, Fig. S4 shows $\Sigma_\gamma^{\rm nor}$ and $\Sigma_\gamma^{\rm ano}$ together with their hidden-fermion fits for the Γ-α component at $U = 8$ and $t_\perp = 2.0$, for three hole concentrations $\delta = 0.025$, 0.1, and 0.2.

At the smallest doping $\delta = 0.025$, both $\Sigma_\gamma^{\rm nor}$ and $\Sigma_\gamma^{\rm ano}$ exhibit pole structures at the particle-hole symmetric pole energies $\omega \simeq \pm 0.7$, which the single hidden-fermion pole [Eqs. (S22) and (S23)] reproduces almost quantitatively. With increasing doping, the pole feature systematically weakens. Since the vertical scale differs between panels, the comparable-looking line shapes, in fact, correspond to a rapid decrease in the absolute magnitude of the pole.

For a large doping ($\delta = 0.2$), the low-energy pole is no longer the dominant feature of the self-energy. The real part of $\Sigma_\gamma^{\rm nor}$ is governed by the smooth, nearly linear background generated by the higher-energy structures (the $-b_{\gamma\mathbf{k}}\,\omega$ term), on top of which the genuine low-energy pole appears only as a weak wiggle. The DCA data develop additional structures away from the pole—a broad background in $\mathrm{Im}\,\Sigma_\gamma^{\rm nor}$ and secondary features around $\omega \simeq \pm 1$ in $\Sigma_\gamma^{\rm ano}$ of magnitude comparable to the central pole—that lie outside the single-pole ansatz and are not captured by the fit. The clean separation of the $\nu = 1$ pole from the remaining structures, on which the single-pole fit relies, is thus gradually lost, and the hidden-fermion pole becomes buried among the other contributions.

S5. DETERMINATION OF THE MI–BI BOUNDARY

In this section, we describe how the phase boundaries at half filling, superimposed in Fig. 2, are determined. In the insulating phase, we estimate the size of the excitation gap from the density of states $A_{\rm tot}(\omega) = \sum_{\gamma,\mathbf{K}} A_\gamma(\mathbf{K},\omega)$ at half filling. To locate the gap edges, we compute the frequency derivative of the spectral function and adopt the local maximum of $|dA_{\rm tot}(\omega)/d\omega|$ closest to $\omega = 0$ as the gap edge, i.e., the energy at which the spectral weight rises most steeply out of the gap region. The excitation gap Δ is then evaluated as the energy difference between the gap edges determined in this way.

Figure S5 shows Δ as a function of $t_\perp$ for several values of U in the insulating regime. For each U, $\Delta(t_\perp)$ exhibits a kink at a certain value of $t_\perp \simeq t_{\perp,c}$, reflecting the change in the character of the insulating gap. We identify this kink with the MI–BI boundary. This criterion is slightly different from that of Ref. [7], where the MI–BI crossover at large U was identified with the point at which the charge gap turns from a decrease to an increase upon increasing $t_\perp$. In the charge-gap data of Ref. [7], however,

TABLE S1. Hidden-fermion parameters in Eqs. (S22) and (S23), used in fitting Fig. S3 for the Γ-α and M-β components at $U = 12$ and $\delta = 0.02$. Since only $V^2_{\gamma\mathbf{k}}$ enters Eqs. (S22) and (S23), we quote $|V_{\gamma\mathbf{k}}|$. The last column lists the self-energy pole energy $E_{\gamma\mathbf{k}} = \sqrt{\varepsilon_{f,\gamma}(\mathbf{k})^2 + D^2_{f,\gamma\mathbf{k}}}$.

		$\lvert V_{\gamma\mathbf{k}}\rvert$	$\varepsilon_{f,\gamma}(\mathbf{k})$	$D_{f,\gamma\mathbf{k}}$	$\tilde{D}_{\mathrm{HE},\gamma\mathbf{k}}$	$\tilde{a}_{\gamma\mathbf{k}}$	$b_{\gamma\mathbf{k}}$	$E_{\gamma\mathbf{k}}$
$t_\perp = 1.0$	Γ-α	4.1218×10^{-1}	-6.8086×10^{-2}	-1.1259×10^{0}	2.1871×10^{-2}	1.5369×10^{0}	8.2592×10^{-1}	1.1279×10^{0}
	M-β	1.3615×10^{0}	-1.0587×10^{-1}	3.7817×10^{-1}	1.4129×10^{0}	2.1043×10^{0}	7.0389×10^{0}	3.9271×10^{-1}
$t_\perp = 1.62$	Γ-α	1.2785×10^{0}	4.6942×10^{-2}	-8.8509×10^{-1}	3.4617×10^{-1}	1.1346×10^{0}	1.9902×10^{0}	8.8634×10^{-1}
	M-β	1.0025×10^{0}	3.1989×10^{-3}	9.1959×10^{-1}	3.7875×10^{-2}	7.6208×10^{-1}	2.1400×10^{0}	9.1959×10^{-1}
$t_\perp = 2.0$	Γ-α	1.6679×10^{0}	-1.1422×10^{-2}	-5.8873×10^{-1}	-3.2640×10^{-1}	1.8274×10^{0}	3.9301×10^{0}	5.8884×10^{-1}
	M-β	5.5842×10^{-1}	2.3868×10^{-1}	1.0625×10^{0}	1.1394×10^{-1}	1.4322×10^{0}	1.1655×10^{0}	1.0890×10^{0}

TABLE S2. Hidden-fermion parameters in Eqs. (S22) and (S23) used in fitting Fig. S4 for the Γ-α component at $U = 8$, $t_\perp = 2.0$, and the hole concentrations $\delta = 0.025$, 0.1, and 0.2. Notations are the same as those in Table S1.

	$\lvert V_{\gamma\mathbf{k}}\rvert$	$\varepsilon_{f,\gamma}(\mathbf{k})$	$D_{f,\gamma\mathbf{k}}$	$\tilde{D}_{\mathrm{HE},\gamma\mathbf{k}}$	$\tilde{a}_{\gamma\mathbf{k}}$	$b_{\gamma\mathbf{k}}$	$E_{\gamma\mathbf{k}}$
$\delta = 0.025$	1.5502×10^{0}	7.0661×10^{-5}	-6.9657×10^{-1}	4.3069×10^{-1}	3.3535×10^{0}	2.0836×10^{0}	6.9657×10^{-1}
$\delta = 0.1$	7.3754×10^{-1}	-1.2361×10^{-1}	-6.8241×10^{-1}	-1.0574×10^{-1}	3.0945×10^{0}	1.2741×10^{0}	6.9351×10^{-1}
$\delta = 0.2$	2.4583×10^{-1}	-1.1717×10^{-1}	4.3543×10^{-1}	1.2193×10^{-1}	2.6172×10^{0}	9.6080×10^{-1}	4.5092×10^{-1}

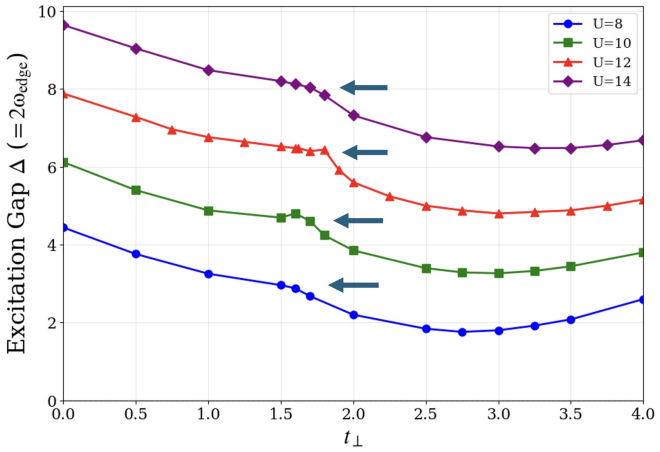

FIG. S5. Excitation gap Δ in the half-filling insulating regime as a function of $t_\perp$, extracted from the spectral functions calculated for $U = 8$, 10, 12, and 14 with varying $t_\perp$. The gap edges are determined from the local maxima of $|dA_{\mathrm{tot}}(\omega)/d\omega|$ near $\omega = 0$. The kink in $\Delta(t_\perp)$ (indicated by arrows) marks the MI–BI boundary.

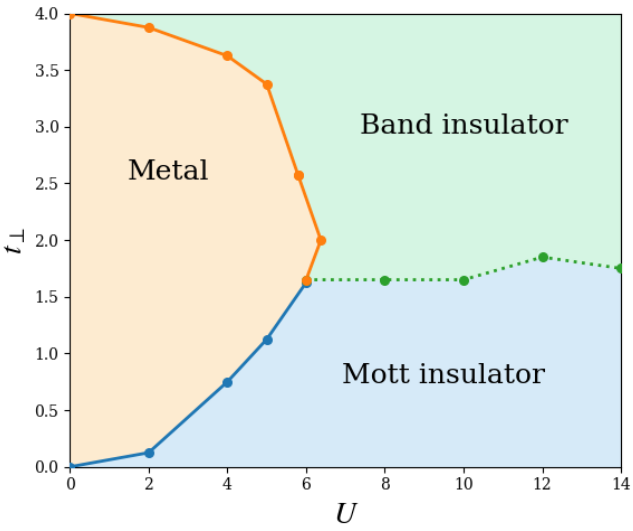

FIG. S6. Phase diagram of the bilayer Hubbard model at half filling in the $(U, t_\perp)$ plane, determined from $\Delta(t_\perp)$. The MI–BI boundary, defined by the kink in $\Delta(t_\perp)$, nearly coincides with the crossing point of the self-energy poles shown in Fig. 1.

this turning point appears as a kink of $\Delta_c(t_\perp)$, i.e., a sharp minimum (at $U = 12t$) or a bend into a nearly flat behavior (at $U = 16t$); identifying the crossover with this feature corresponds to the boundary defined here, and the two ways of determining the boundary are therefore consistent with each other. Notably, the position of the kink almost coincides with the crossing point of the self-energy poles of the Γ-α and M-β components discussed in the main text [e.g., $t_\perp \simeq 1.62$ at $U = 12$; see Fig. 1], corroborating that the MI–BI crossover is governed by the rearrangement of the low-energy self-energy poles. The phase diagram thus obtained is shown in Fig. S6.

S6. DOPING DEPENDENCE OF THE SUPERCONDUCTING ORDER PARAMETER

In the main text, the superconducting order parameters are shown at $\delta = 0.02$ [Fig. 2], where both Γ-α and M-β components are largest near the crossing point of the metal–insulator boundary and the MI–BI boundary. To examine how this distribution evolves with doping, Fig. S7 shows the corresponding $(U, t_\perp)$ maps of the Γ-α and M-β order parameters at a larger doping $\delta = 0.05$, with the half-filling phase diagram (Sec. S5) superimposed.

The order parameters retain the $s^{\pm}$ character found at $\delta = 0.02$: the Γ-α and M-β components carry opposite signs [$\langle c^{\alpha}_{\Gamma\uparrow} c^{\alpha}_{\Gamma\downarrow}\rangle < 0$ and $\langle c^{\beta}_{\mathrm{M}\uparrow} c^{\beta}_{\mathrm{M}\downarrow}\rangle > 0$]. Moreover, the region where the superconductivity emerges is almost unchanged from $\delta = 0.02$: both components are concentrated in a horizontal stripe centered on the MI–BI boundary, which nearly coincides with the pole crossing $t_{\perp} \simeq t_{\perp,c}$ discussed in the main text.

The main difference from $\delta = 0.02$ thus lies in the distribution of the order-parameter magnitude within this stripe: while the largest values are still found near the metal–insulator boundary, sizable values now extend along the MI–BI boundary toward larger U values. This behavior can be interpreted in terms of the doping dependence of the hidden-fermion pole (see Fig. S4 and Table S2): with increasing doping, the intensity of the low-energy self-energy poles decreases, so that the dynamical pairing enhancement driven by these poles weakens and the pairing approaches a more conventional, BCS-like static one. The weakened enhancement around the metal–insulator boundary results in relatively large values of the order parameters at large U. This trend may also be regarded as reflecting the doping-induced crossover from a BEC-like to a BCS-like superconducting state reported for the bilayer Hubbard model in Ref. [8].

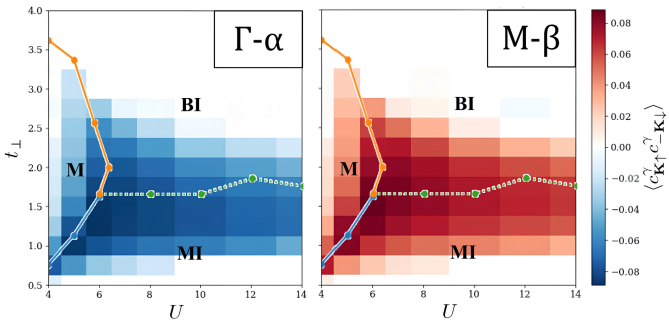

FIG. S7. Superconducting order parameters in the $(U, t_{\perp})$ plane at $\delta = 0.05$ for the Γ-α component [$\langle c^{\alpha}_{\Gamma\uparrow} c^{\alpha}_{\Gamma\downarrow}\rangle$, left] and the M-$\beta$ component [$\langle c^{\beta}_{\mathrm{M}\uparrow} c^{\beta}_{\mathrm{M}\downarrow}\rangle$, right], on a common color scale; the opposite signs (Γ-$\alpha < 0$: blue, M-$\beta > 0$: red) indicate $s^{\pm}$-wave symmetry. The half-filling phase diagram (M: metal, MI: Mott insulator, BI: band insulator) and its boundaries (from Sec. S5), including the MI–BI boundary (green dashed curve), are superimposed. Compared with $\delta = 0.02$ (Fig. 2), the region of large order parameter extends along the MI–BI boundary toward the strongly correlated (large-U) side.

[1] M. H. Hettler, A. N. Tahvildar-Zadeh, M. Jarrell, T. Pruschke, and H. R. Krishnamurthy, Phys. Rev. B **58**, R7475 (1998).
[2] T. Maier, M. Jarrell, T. Pruschke, and M. H. Hettler, Rev. Mod. Phys. **77**, 1027 (2005).
[3] E. R. Gagliano and C. A. Balseiro, Phys. Rev. Lett. **59**, 2999 (1987).
[4] S. Sakai, M. Civelli, and M. Imada, Phys. Rev. Lett. **116**, 057003 (2016).
[5] S. Sakai, M. Civelli, and M. Imada, Phys. Rev. B **94**, 115130 (2016).
[6] S. Sakai, J. Phys. Soc. Jpn. **92**, 092001 (2023).
[7] S. S. Kancharla and S. Okamoto, Phys. Rev. B **75**, 193103 (2007).
[8] Y. Nomura, M. Kitatani, S. Sakai, and R. Arita, Phys. Rev. B **112**, L020504 (2025).